RSC Advances

PAPER

View Article Online
View Journal | View Issue

Cite this: *RSC Adv.*, 2017, 7, 20219

A biomolecule-assisted, cost-efficient route for growing tunable $CuInS_2$ films for green energy application†

Anna Frank,‡[a] Angela S. Wochnik,‡[b] Thomas Bein[b] and Christina Scheu *[ac]

$CuInS_2$ has become a popular and promising candidate as an absorber material in photovoltaic devices and photo-electrochemical cells. Here we report the successful L-cysteine-assisted growth of homogeneous, nanostructured $CuInS_2$ thin films deposited on fluorine-doped tin oxide coated glass. In contrast to existing synthesis routes using thioacetamide as a sulfur source, our method offers the advantage of being environmentally friendly and non-toxic. We found that L-cysteine is able to reduce the Cu^{2+} ions of the precursor $CuSO_4$ to Cu^+ in aqueous solution, thus enabling the formation of $CuInS_2$ thin films. By varying the concentration of the reaction solution during the solvothermal synthesis route, we obtained $CuInS_2$ films with different thicknesses and compositions, investigated with the help of energy dispersive X-ray spectroscopy with scanning and transmission electron microscopy. X-ray and electron diffraction experiments of the films prove the synthesis of a pure $CuInS_2$ phase with the chalcopyrite structure except for the highest L-cysteine concentration where additional In_2S_3 forms. UV-Vis absorption spectroscopy reveals absorption over the whole visible spectrum. The calculated band gap using the UV-Vis data ranges between 1.4 and 1.5 eV, and can be adjusted by changing crystal size and chemical composition. This offers a promising route towards tuning the optical and transport properties. First dye degradation experiments show promising activity under solar illumination.

Received 24th November 2016
Accepted 3rd April 2017

DOI: 10.1039/c6ra27294k

rsc.li/rsc-advances

Introduction

In recent years, the development of alternative semiconductor materials for photophysical and photochemical applications such as solar cells and solar-driven hydrogen production has become a very active research field. The requirements for these materials include (cost-) efficient manufacturing processes, as well as low toxicity of the synthesis and the material itself. These features can be found in copper indium disulfide ($CuInS_2$), which became one of the most popular and promising candidates for absorber materials in photovoltaic and photochemical applications. Advantages of this material include its good long-term stability, a high absorption coefficient ($\alpha \approx 10^5$ cm^{-1}) and a direct band gap of 1.5 eV.[1] Compared to the commonly used $CuInSe_2$, it is not toxic[2] and has a high chemical stability.[3] Furthermore, the type of conductivity can be tuned depending on the chemical composition.[4] Known manufacturing processes include chemical vapor deposition,[5] spray pyrolysis[6] and electro-deposition.[7] However, these methods are rather expensive. Therefore, synthesis of $CuInS_2$ films *via* cost-efficient methods such as chemical bath deposition,[8] successive ionic layer deposition,[9] microwave assisted growth,[10] hot-injection,[11] sol–gel methods[12] and mild solvothermal synthesis routes[13,14] has attracted increasing attention. In previous reports,[15,16] we have presented the synthesis of $CuInS_2$ thin films and microspheres using a one-step, cost-efficient solvothermal method that had been developed by Peng *et al.*[13] and further modified in our studies. This method makes it possible to directly grow thin films on a suitable substrate without the need to deposit the material after synthesis. Depending on the reagent stoichiometry and thermal treatments, we were able to synthesize $CuInS_2$ films with different thicknesses and morphologies, using thioacetamide as the sulfur source.[15,16] However, thioacetamide is a toxic and carcinogenic substance. Hence, to prepare $CuInS_2$ thin films *via* a non-toxic route, we changed the sulfur source to the biomolecule L-cysteine, an amino acid.

Biomolecule-assisted synthesis has proven to be a novel, environmentally friendly and promising method to prepare various nanomaterials, making use of the unique features of biomolecules including the capability to engage in self-assembly processes.[17] Biomaterials such as DNA, (poly) peptides and amino acids have been used to control the size and

---

[a] *Max-Planck-Institut für Eisenforschung GmbH, Max-Planck-Straße 1, 40237 Düsseldorf, Germany. E-mail: scheu@mpie.de*

[b] *Department of Chemistry, Center for NanoScience (CeNS), Ludwig-Maximilians-Universität, Butenandtstrasse 5-11 (E), Munich, Germany*

[c] *Materials Analytics, RWTH Aachen University, Kopernikusstr 10, 52074 Aachen, Germany*

† Electronic supplementary information (ESI) available. See DOI: 10.1039/c6ra27294k

‡ Contributed equally.

shape of various nanomaterials.[18–20] L-Cysteine [Cys, $HSCH_2$-$CH(NH_2)COOH$] is a thiol-containing amino acid that is inexpensive and environmentally friendly. Additionally, it has a strong affinity towards metal ions to form metal–ligand complexes and can therefore not only act as sulfur source but also as structure directing agent in the synthesis of (not only) sulfidic nanocrystals.[20–22] Previously reported L-cysteine-assisted synthesis strategies involving solvothermal processes include Bi_2S_3, In_2S_3, CuS, PbS, $AgBiS_2$, TiO_2, $ZnIn_2S_4$, Cu_2CoSnS_4 and $CuInS_2$ nanocrystals.[17,23–31]

$CuInS_2$ nanocrystals have been synthesized by Liu *et al. via* a L-cysteine-assisted solvothermal process.[17] They obtained a product containing agglomerations of irregular microspheres and nanocrystals. Wen *et al.*[31] produced $CuInS_2$ powders using L-cysteine as sulfur source. The powders consisted of microspheres made up of nanosheets. To the best of our knowledge, there have been no reports on the direct growth of $CuInS_2$ thin films on transparent, conductive substrates using L-cysteine as the sulfur source. The electrodes fabricated in this way are of interest for application in photoelectrochemical and solar cells.

Herein we report about a solvothermal synthesis strategy that allows for preparing $CuInS_2$ films directly on fluorine-doped tin oxide (FTO) conductive glass substrates by involving the non-toxic biomolecule L-cysteine. This method enabled us to achieve homogeneous coverage of the FTO substrate, which is a prerequisite for photovoltaic and photoelectrochemical applications. Moreover, the concentration of reactants can be varied to control not only the thickness but also the composition and grain size which directly affect the optical and electrical properties.

Experimental section

Synthesis of $CuInS_2$ films

All reagents were of analytical grade and were used without further purification. FTO conductive glass (Sigma-Aldrich) with dimensions of 15 × 20 × 2 mm was used as substrate for the deposition of the $CuInS_2$ films. All substrates were washed before use in dilute nitric acid, double-distilled water, acetone and ethanol in an ultrasonic cleaner for 5 min respectively. Peng *et al.*[13] dissolved $CuSO_4\cdot5H_2O$, $InCl_3\cdot4H_2O$ and thioacetamide in ethanol and stirred it for 15 min. Afterwards, they placed an FTO substrate in a Teflon-lined stainless steel autoclave and kept it in an oven for 12 h at 160 °C. This procedure was modified in our previous work and a lower temperature was found to be sufficient.[15,16] In the present work we changed the sulfur source from thioacetamide to L-cysteine. Three films were prepared using different concentrations of reactants, hereafter referred to as films A, B and C (see Table 1).

In a Teflon liner (20 ml capacity), $CuSO_4\cdot5H_2O$ and $InCl_3$ were dissolved in 10 ml ethanol and stirred for 10 min. Subsequently, L-cysteine was added and the reaction solution was stirred for another 5 min, resulting in a pH of the reaction solution of around 5, which is the isoelectric point of L-cysteine. For the different reactant concentrations see Table 1. The cleaned FTO substrates were placed in the Teflon liner and the sealed stainless-steel autoclave was heated to 150 °C and kept at this temperature for 18 h. After the reaction the autoclave was left to cool down to room temperature, the obtained films were washed using ethanol and double-distilled water, and dried with compressed air. Samples were stored at ambient conditions.

Table 1 Concentrations of reactants used to synthesize films A, B and C. The reaction temperature and time are 150 °C and 18 h, respectively

		$CuSO_4\cdot5H_2O$	$InCl_3$	L-Cysteine
Film A	Mass [g]	0.075	0.066	0.145
	Amount [mol]	0.3	0.3	1.2
	Molarity [M]	0.03	0.03	0.12
	Normalized	1	1	4
Film B	Mass [g]	0.050	0.044	0.061
	Amount [mol]	0.2	0.2	0.5
	Molarity [M]	0.02	0.02	0.05
	Normalized	1	1	2.5
Film C	Mass [g]	0.025	0.022	0.036
	Amount [mol]	0.1	0.1	0.3
	Molarity [M]	0.01	0.01	0.03
	Normalized	1	1	3

To investigate whether L-cysteine can reduce Cu^{2+} to Cu^+, the precursors $CuSO_4\cdot5H_2O$ and L-cysteine were brought to reaction in 10 ml ethanol for 18 h at RT. The resulting grey solid was filtered and washed with ethanol, double-distilled water and dried in air. For comparison, $CuSO_4\cdot5H_2O$ and L-cysteine were also heated to 150 °C and hold at this temperature for 18 h, following a procedure from Li *et al.*[25]

Characterization

The crystal structure of the films was determined by X-ray diffraction (XRD) acquired with a diffractometer of a Seifert Type ID3003 X-ray generator, equipped with a scintillation counter, using Co K_α radiation and an Fe-filter ($\lambda = 1.79$ Å). The scanning rate was $0.05°\ s^{-1}$ with a count time of 30 s per step and a 2θ range from 20 to 130°. The obtained patterns were compared to literature data (see ESI Table 1†). Average crystallite size was calculated using the Scherrer equation.[32] For this purpose the (112) and (204) peaks were fitted by using a Gaussian function.

The morphology was investigated by scanning electron microscopy (SEM) using a ZEISS Merlin operated at 5.0 kV and a probe current of 2.0 nA. Secondary electron (SE) imaging was done using the attached InLens® ZEISS standard detector. The samples were palladium/gold coated prior to the insertion into the SEM. The average chemical composition was analyzed by energy dispersive X-ray (EDX) spectroscopy using the XFlash detector 6|30 from Bruker. EDX was performed at 20.0 kV and a probe current of 4.0 nA. Analysis was done with the Bruker Esprit 1.9.4.5 software and the obtained atomic ratios were normalized relative to copper. Cross sections were prepared for the investigation of the film thickness and images were taken with a focused ion beam (FIB) FEI Helios Nanolab 600. For cutting the samples *via* FIB, the samples were coated with conductive silver paint to avoid destruction of the sample surface.

For further characterization, (scanning) transmission electron microscopy ((S)TEM) investigations were performed. These were done on an FEI Titan Themis 300 (S)TEM microscope operated at an acceleration voltage of 300 kV and equipped with a C_S probe corrector, a Gatan Quantum ERS image filter and a Super X-EDX detector from Bruker. Electron diffraction data were evaluated using a calibrated camera constant obtained from a Si standard. Dual electron energy loss spectroscopy (EELS) was also performed at the FEI Titan Themis using a dispersion of 0.1 eV per channel and an acceleration voltage of 60 kV. This allowed us to study the S-$L_{2,3}$ edge at around 165 eV and the Cu-$L_{2,3}$ edge at around 930 eV with a sufficient signal-to-noise ratio.

UV-Vis absorption measurements of the films were done on a Perkin Elmer Lambda 1050 in transmission mode within a spectral region of 250 to 1200 nm (step size 1 nm). The band gap was determined from the UV-Vis data using the Tauc method for direct band gap semiconductors.[33] UV-Vis measurements for dye degradation experiments have been performed on a Perkin Elmer Lambda 800 in absorption mode in a range from 260 to 900 nm (also with a step size of 1 nm). Dye degradation has been studied using the dye rhodamine B, solved in water, and under illumination with one sun using a solar simulator.

Results

Fig. 1 shows SE images of the three films synthesized with different concentrations of reactants but using the same reaction temperature and time (150 °C for 18 h). For all films the ratio between Cu and In was 1 : 1. For film A the highest amount of sulfur was used to investigate the influence of sulfur. The molar amount of the other precursors was adjusted. For film B and C the same sulfur to copper/indium ratio was used (within the measurement accuracy). The amount of the precursors was doubled for film B compared to film C which should result in different thicknesses of the films. All films grow homogeneously on the FTO substrate and cover it completely. No cracks or delamination of the film could be observed.

Film A, which exhibits a dark brown color, was synthesized with the highest concentration of 0.03 : 0.03 : 0.12 M Cu : In : S

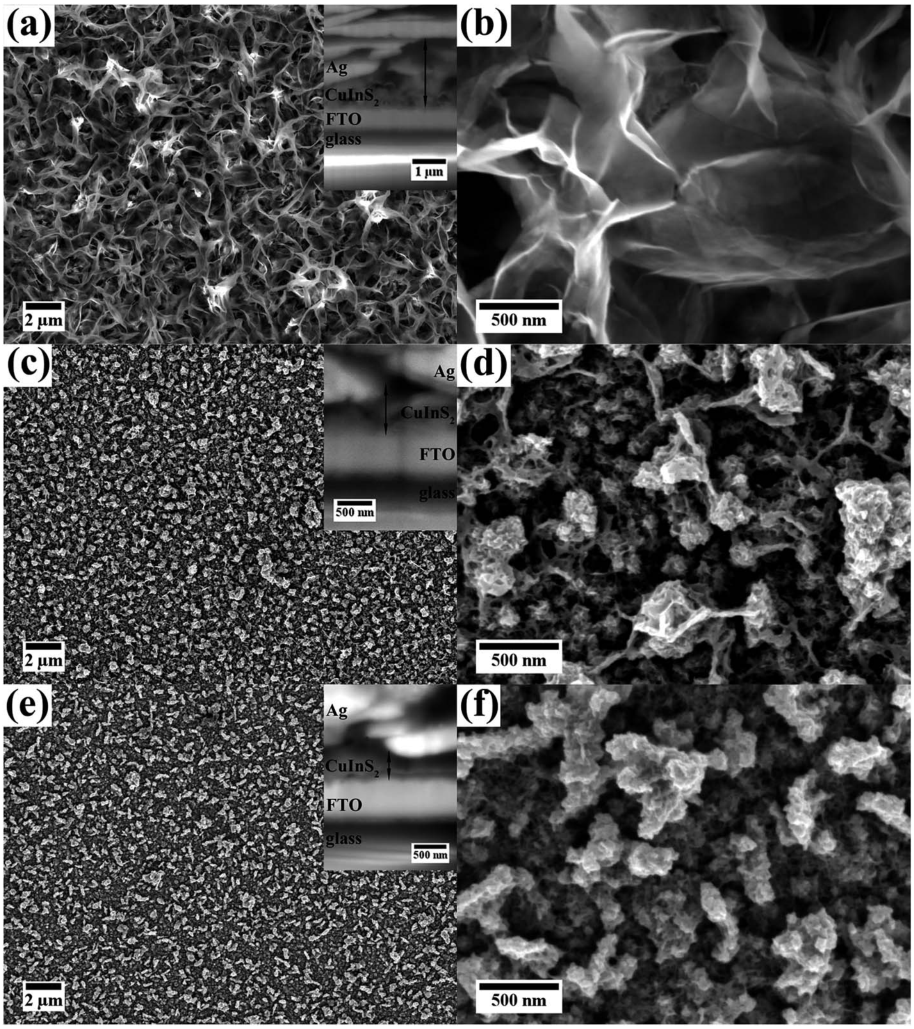

Fig. 1 Top view SE images of three $CuInS_2$ films synthesized with different concentrations of reactants on FTO substrates at different magnifications. Images (a) and (b) show film A. Images (c) and (d) are taken from film B. Images (e) and (f) display film C. FIB cross sections of the different films are shown as insets in (a), (c) and (e).

and the highest sulfur content, at a nominal Cu : In : S precursor ratio of 1 : 1 : 4 (Fig. 1(a) and (b)). The top layer of the film consists of nanoplates. At higher magnification (Fig. 1(b)) the thin, plate-like structures are better visible. The cross-sectional SE image and the TEM investigations described below reveal the presence of a compact layer in contact to the FTO substrate. The underlying FTO substrate cannot be observed in top view indicating that the $CuInS_2$ is completely covering the substrate. The complete film shows a thickness of up to 1.6 μm with partly thinner parts due to varying dimensions of the nanoplates.

SEM images of film B, which displays a brown color, are presented in Fig. 1(c) and (d). This film was synthesized with a lower precursor concentration than film A (only 0.02 : 0.02 : 0.05 M) and a nominal precursor ratio of Cu : In : S 1 : 1 : 2.5. The film consists of a more dense film with agglomerates on top, which are more loosely packed. Fig. 1(d) (taken at higher magnification) reveals that the film is built up of small $CuInS_2$ nanoparticles. As for film A thin, plate-like structures are visible, although not as pronounced. The thin plates seem to connect the agglomerates. The thickness of the film is around 450 nm with thicker parts due to agglomerates on the surface (up to 700 nm).

Film C has a bright brown color and was synthesized with the lowest concentration of precursors (0.01 : 0.01 : 0.03 M, Cu : In : S 1 : 1 : 3). This film possesses a surface structure similar to film B, but contains less large agglomerates on top of the film which consist, close to the substrate, of small nanoparticles (Fig. 1(e) and (f)). Thin plate-like features, as for film A and B, cannot be observed. The film thickness is estimated to be around 350 nm with agglomerates sized up to 500 nm.

Comparing the three films, it becomes clear that the molarity of the precursors strongly affects the thickness of the film. The S content of the precursor solution has an influence on the morphology.

The average chemical composition of the films was measured using EDX in SEM. The spectra of all films reveal signals of Cu, In, and S and weaker signals of Sn, Si and O. The detected Sn originates from the FTO substrate and the Si from the glass. The oxygen can stem from FTO or glass. No additional peaks indicating impurities were observed. The appearance of Sn, O and Si signals and the small thickness of the films lead to significant errors in quantification. In addition, the In L and Sn L X-ray energies overlap (see ESI Fig. 1†) which leads to difficulties in the quantification. For this reason EDX measurements have been performed in the STEM where the influence of the FTO substrate leading to the Sn signal can be neglected. SEM EDX quantification results of the films A, B and C are summarized in ESI Table 2.†

The crystal structure of the films was investigated on a global scale *via* XRD. The XRD patterns of the films possess the characteristic reflections of $CuInS_2$ in the chalcopyrite structure (Fig. 2). Chalcopyrite is a tetragonal crystal structure with lattice parameters $a = 0.552$ nm and $c = 1.112$ nm. The observed $CuInS_2$ reflections and all additional reflections originating from the FTO substrate are marked in the pattern (ESI Table 1†). As can be seen, the intensity of the $CuInS_2$ peaks of film A is higher than for film B and C, in accordance with the greater thickness of the film.

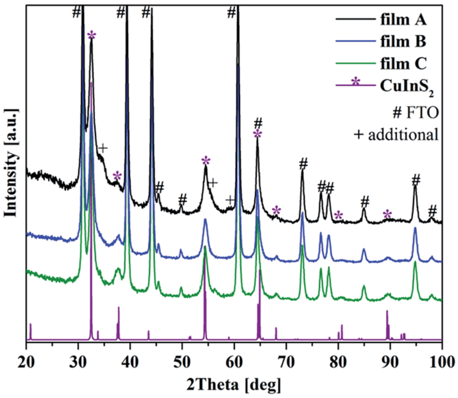

Fig. 2 XRD patterns of film A, B and C reveal the tetragonal chalcopyrite crystal structure (*). Additional peaks result from the FTO substrate (#). In case of film A reflections originating from In_2S_3 are observed (+).

For film A (highest overall concentration as well as highest sulfur content) a few additional reflections, compared to the pattern of film B and C, can be observed. Particularly, there are peaks at around 34.2°, 55.6° and 59.2°. These reflections can arise from $CuInS_2$ in the wurtzite modification ((101) at 34.2° and (103) at 59.2°) or from In_2S_3, which crystallizes in a distorted tetragonal crystal structure ((206) at 34.2°, (2 2 12) at 55.6° and (329) at 59.2°). The used literature data are summarized in ESI Table 1.† Other possible reflections of these phases overlap either by the chalcopyrite peaks or the peaks arising from the FTO substrate. Coexistence of chalcopyrite and wurtzite modifications of $CuInS_2$ has been observed before.[16,34] However, due to the TEM results described below we exclude the presence of $CuInS_2$ in wurtzite crystal structure and attribute the additional peaks to the presence of In_2S_3. In_2S_3 thin films, also prepared solvothermally on FTO substrates, have a very similar appearance compared to the surface structure of our film A.[35] For the XRD patterns of film B and C the mentioned peaks are not present.

Other byproducts or impurities such as copper sulfides or their oxides were not observed. However, their presence cannot be fully excluded because of the low intensity of the $CuInS_2$ reflections compared to the strong signals of the highly crystalline FTO substrate and the rather broad peaks for $CuInS_2$ due to the small size of the crystals. Beside this all the phases show very similar *d*-values and can therefore lead to overlapping peaks.

The $CuInS_2$ peaks are rather broad, indicating that small domain or crystal sizes occur in the film structures. These were analyzed by applying the Scherrer equation using a K shape factor of 0.9 for the most intense $CuInS_2$ peaks (112) and (204).[32] Average values were obtained from evaluating both peaks. The calculations resulted in an average crystallite size of 10 nm ± 1 nm for all films. More precise crystal size investigation was done on high-resolution TEM images (see below).

The absorption behavior of the films was studied using UV-Vis spectroscopy. The spectra of film A (line), film B (dashed) and film C (dotted) are given in Fig. 3(a). In all cases, the spectra display absorption over the whole visible spectrum. The highest absorption is obtained for film A, which was synthesized with the highest concentration of precursors and shows the highest film thickness of 1.6 μm. Film B and film C also show significant absorption. Due to similar thickness (in the range of 300–500 nm) they show a similar absorption. In general, the absorbance increases linearly with the film thickness.

The band gap was calculated from the UV-Vis data using the Tauc method. As an example, the region of the linear fit is marked in Fig. 3 (b, film B). For film A a band gap of 1.43 eV, for film B 1.47 eV and for film C 1.40 eV was estimated. These values are close but lower than the ones mentioned in the literature for the bulk material as well as those reported for nanostructures.[1,36] The reason for our band gaps being smaller might be related to the small crystallite size and a corresponding large number of defects in the crystal structure, as well as to differences in composition. This will be discussed in more detail later.

The Urbach tails, visible in the region of the linear fit, have been observed before for $CuInS_2$; they have been attributed to sub-band gap excitations that are related to the defects in the crystal structure and influenced by the chemical composition.[37–39] Our films possess small grains which means that a large number of grain boundaries are present in the films. Therefore we assume that the polycrystalline character and the large number of grain boundaries as well as interfaces are the reason for the observed Urbach tails.

(S)TEM investigations were done for all films to determine layer thickness, crystallite size, local crystal structure and chemical composition at the nanometer scale. To do so, films were removed from the substrate and deposited on holey-carbon coated Au grids. This way an influence of the sample preparation on the measurements, especially EDX, can be excluded. A collection of high-resolution TEM images and diffraction patterns is given in Fig. 4 and 5. EDX analysis of all the films was done in STEM mode with a spot size in the range of 1 nm. Data were collected by acquiring EDX maps at different regions and quantification was done for various areas of these maps.

In the SEM film A with the highest concentration of precursors (0.03 : 0.03 : 0.12 M, nominal Cu : In : S precursor ratio 1 : 1 : 4) showed a layer of nanoplates, connected to each other (see Fig. 1). These nanoflakes can also be observed in the TEM (Fig. 4). The TEM images show a more compact part of the film (bottom layer) with outgrowing nanoflakes (surface layer). The flaky structure seems so consists of darker appearing rods with outgrowing flakes. These flakes then interconnect with each other and other rods. While acquiring EDX data it became obvious that the film consists of a Cu rich bottom layer and an In rich surface layer which forms the in the top view SEM observed flakes (an exemplary EDX map is shown in the ESI Fig. 2†). EDX spectra acquired in STEM mode on film A reveal 12 ± 4 at% Cu, 34 ± 3 at% In and 54 ± 4 at% S for the surface layer giving a ratio of 1.0 : 3.0 : 4.8. This ratio is drastically deficient in Cu and therefore confirms the presence of In_2S_3, with some Cu incorporated. In_2S_3 was also detected by XRD. As mentioned before, In_2S_3 can be synthesized solvothermally using L-cysteine, resulting in a very similar topology.[35] High-resolution TEM images and electron diffraction pattern taken from only a flaky area as well as from an area with both flakes and rods prove the (poly) crystallinity of the surface layer. Considering the EDX measurements which show a very low amount of copper the electron diffraction pattern in Fig. 4(c) and (d) have been indexed according to tetragonal In_2S_3.[40] The coexistence of other phases such as $CuInS_2$ and Cu_2S cannot be excluded (for comparison of *d*-values see ESI Table 1†).

In the STEM EDX measurement the bottom layer of film A gives 22 ± 4 at% Cu, 28 ± 4 at% In and 50 ± 6 at% S, meaning a ratio of 1.0 : 1.3 : 2.3 which is close to the stoichiometric ratio of Cu : In : S 1 : 1 : 2 but slightly In and S rich. In Fig. 5(a) and (b) a high-resolution TEM image as well as a diffraction pattern of the bottom layer can be found. It becomes clear that the bottom layer of film A is built up of small nanocrystals which agglomerate to form a more compact layer of $CuInS_2$. Single crystallites are exemplarily marked in Fig. 5(a). The average size of the nanoparticles is 6.3 ± 2.6 nm. The electron diffraction pattern (Fig. 5(b)) shows polycrystallinity and can be indexed according to the tetragonal $CuInS_2$ phase with *d*-values of (112), (204)/(220), (301) and (116)/(312) as well as tetragonal In_2S_3 and its (200)/(116), (211), (213)/(109), (2 0 14), (329)/(413) and (420)/(336) planes. The presence of $CuInS_2$ in the hexagonal wurtzite modification cannot be excluded ((100), (002), (110), (103) and (112)). Furthermore, as mentioned before Cu(I)-sulfides show

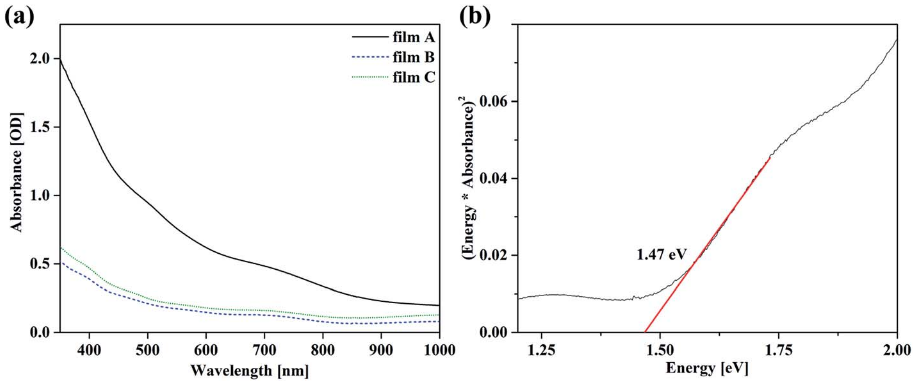

Fig. 3 (a) UV-Vis spectra of film A (line), B (dashed) and C (dotted). In (b) an exemplary Tauc plot is shown, indicating a band gap of 1.47 eV for film B.

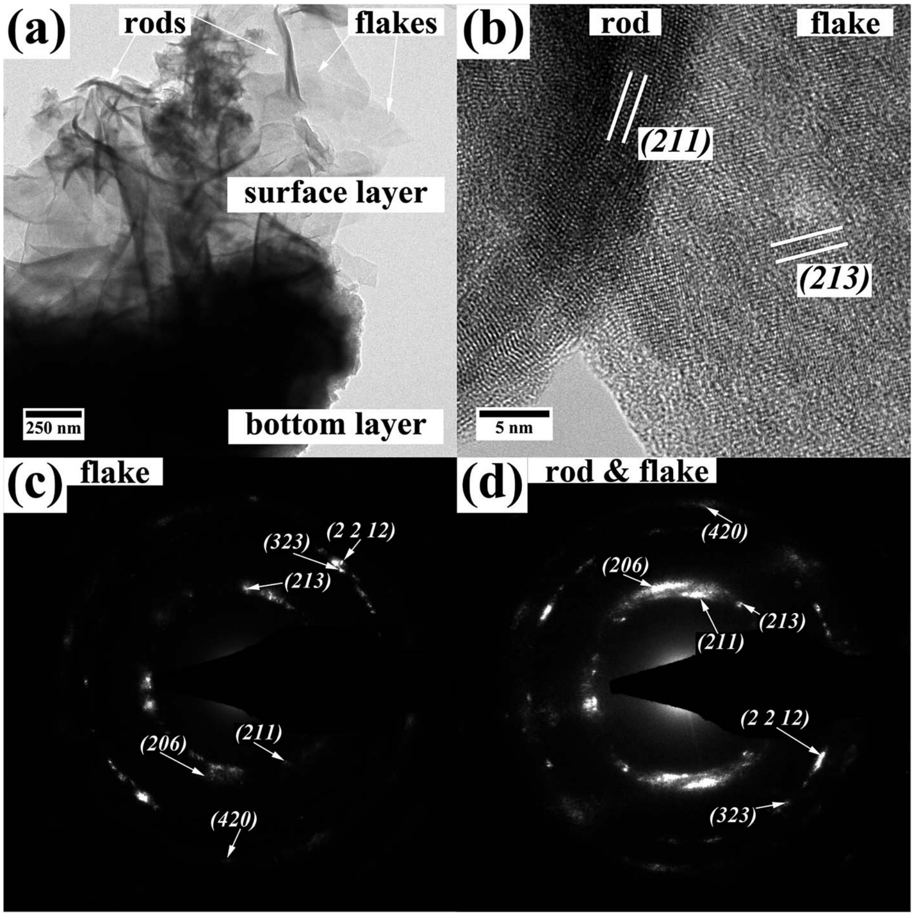

Fig. 4 TEM images (a), (b) and electron diffraction pattern (c), (d) of the top layer of a sample prepared from film A. The electron diffraction pattern can be indexed according to tetragonal In_2S_3.[40]

similar *d*-values (see ESI Table 1†) but their presence can be excluded by the EDX measurements. The phase diagram of the (Cu–In–S)-system resulting from a quasi-binary system of Cu_2S–In_2S_3 indicates the predominant formation of $CuInS_2$ in the chalcopyrite structure with around 50 to 52% mole percent In_2S_3 for the given conditions.[41] As we used Cu and In in equimolar composition, we assume that the system is in that region of the phase diagram.

The (S)TEM investigations of film B (medium concentration of precursors, 0.2 : 0.2 : 0.5, nominal Cu : In : S precursor ratio 1 : 1 : 2.5, Fig. 5(c) and (d)) give similar results as for the bottom layer of film A. They reveal a layer of $CuInS_2$ which consists of agglomerated nanoparticles. Again, high resolution TEM imaging and electron diffraction demonstrate the polycrystallinity of the as-synthesized $CuInS_2$ layer and show no obvious reflections of any side product like Cu or In sulfides. In rich areas as described for film A (surface nanoflake layer) cannot be observed. The average crystallite size is 5.3 ± 2.2 nm. EDX gives 24 ± 2 at% Cu, 25 ± 2 at% In and 51 ± 3 at% S. The Cu : In : S ratio is 1.0 : 1.0 : 2.1, which is very close to a stoichiometric composition.

For the lowest concentration of precursors (film C, 0.1 : 0.1 : 0.3, nominal Cu : In : S precursor ratio 1 : 1 : 3, Fig. 5(e)–(f)) electron diffraction and high resolution TEM show that the film is crystalline, too. For this film the crystal size is 4.9 ± 2.0 nm. The EDX analysis gives 26 ± 2 at% Cu, 24 ± 2 at% In and 51 ± 3 at% S which results in Cu : In : S 1.0 : 0.9 : 2.0. As for film B this is also very close to a stoichiometric composition of $CuInS_2$.

However, as already mentioned the presence of other side products like In_2S_3 or Cu^I sulfides cannot be fully excluded because of the very similar *d*-values of the compounds (see ESI Table 1†). Nevertheless, because in the XRD pattern of film B and C no reflections of such byproducts can be found and the EDX measurements show stoichiometric $CuInS_2$ quantification we assume that the presence of In_2S_3 and Cu_2S can be neglected for films B and C.

To investigate the growth mechanism of the films, the reaction of L-cysteine with $CuSO_4$ was analyzed. When L-cysteine and $CuSO_4$ are dissolved in ethanol, a grey solid is formed after stirring for 18 h at room temperature (RT). The XRD pattern reveals many reflections (see Fig. 6(a)). The most intense reflections correspond to crystalline, hexagonal L-cystine ($a = 0.54$ nm, $c = 5.59$ nm), which is formed during the reaction between L-cysteine and Cu^{2+} in the reaction solution (see also Fig. 9 in the Discussion section).[25,42] Other reflections match well with a Cu–cysteine complex in a monoclinic crystal structure with the lattice parameters $a = 1.41$ nm, $b = 0.45$ nm and $c = 0.98$ nm as described by Dokken *et al.*[43] Additionally, weak reflections of Cu_2S can be found in the XRD spectrum

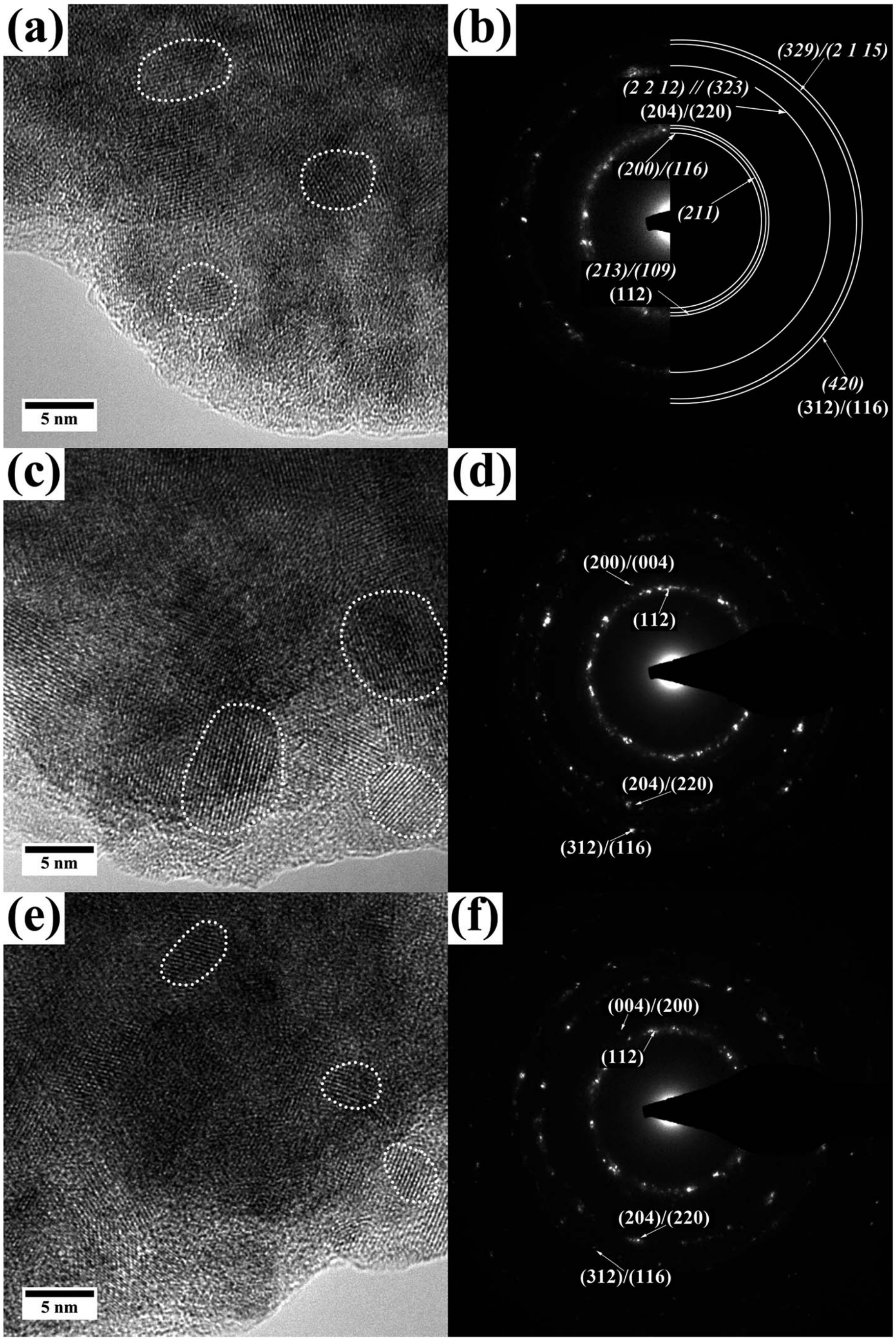

Fig. 5 TEM images of the synthesized $CuInS_2$ samples. Panels (a and b), film A. Panels (c and d), film B. Panels (e and f), film C. Panels (a), (c) and (e) show the HRTEM images of the samples of film A, B and C, respectively. Panels (b), (d) and (f) show the related electron diffraction patterns and prove polycrystallinity of the samples. Reflections originating from In_2S_3 are in italic writing.

(Fig. 6).[44,45] The intense background is due to the presence of an amorphous phase, *e.g.*, non-crystalline Cu cysteine complexes or remaining precursors.

Furthermore, L-cysteine and $CuSO_4$ were brought to reaction for 18 h at 150 °C. The resulting black powder was also analyzed with XRD, and the pattern shows reflections that all fit well to hexagonal CuS. No additional reflections were observed.

(S)TEM analysis of the grey solid shows 1.5–5 nm sized crystals embedded in an amorphous material. The high-resolution TEM and BF images are given in Fig. 7(a) and (b). The electron diffraction pattern reveals reflections with *d* values of 3.4 Å, 3.2 Å, 1.9 Å and 1.6 Å and a polycrystalline character of the sample. These values can be assigned to (0 0 −18), (0 2 16)/(0 2 14) and (−1 3 18) of L-cystine and to Cu^I cysteine complexes, but also to (102), (202)//(114)/(200) and (213) of Cu_2S in the tetragonal structure, as well as to the (100)//(102), (110)//(103) and (004) reflections of Cu_2S in the hexagonal structure (diffraction pattern shown in Fig. 7(c), the corresponding values

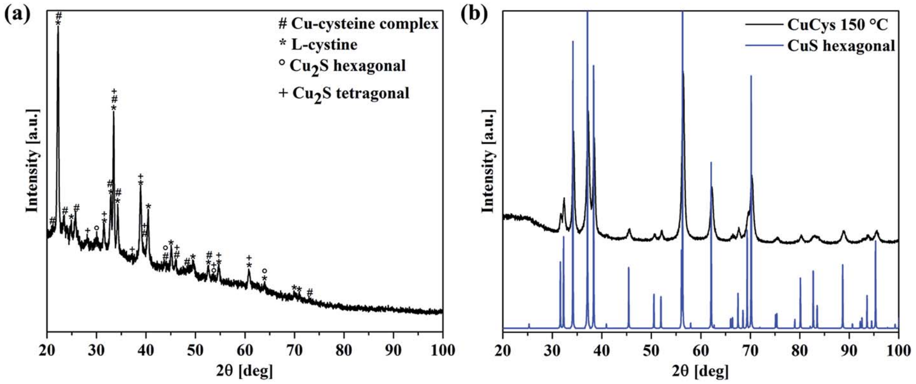

Fig. 6 (a) XRD pattern of the grey reaction product of L-cysteine and $CuSO_4$ stirred for 18 h at RT. The measured pattern is a mixture of crystalline L-cystine[42] (marked with *) and Cu–cysteine complexes (marked with #) as published by Dokken *et al.*[46] The presence of hexagonal or tetragonal Cu_2S cannot be excluded (marked with ° and +, respectively). (b) XRD pattern of L-cysteine and $CuSO_4$ reacted at 150 °C for 18 h. Every reflection fits well with a hexagonal CuS phase.[47]

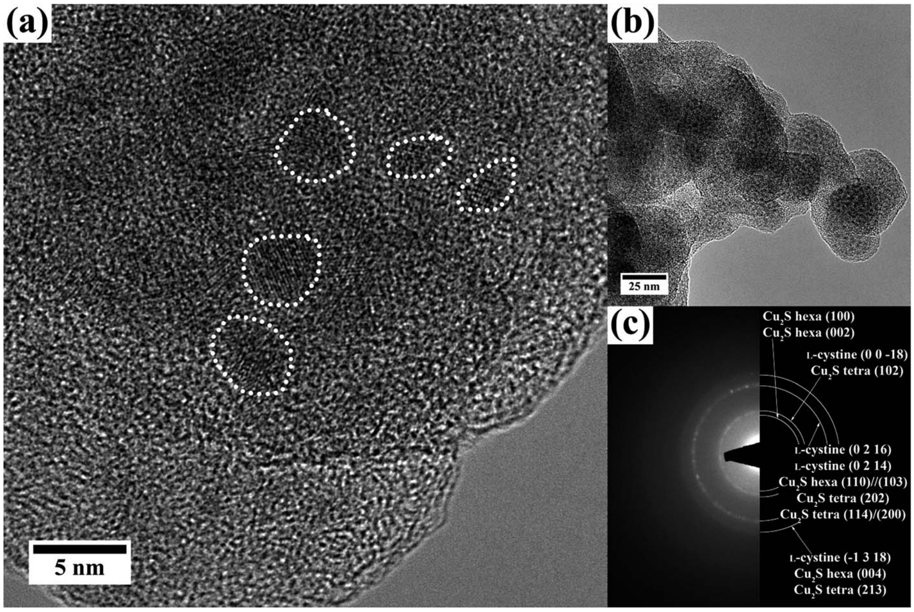

Fig. 7 (a) High resolution TEM image of the reaction product of L-cysteine and $CuSO_4$ in ethanol shows 1.5–5 nm sized crystals (exemplarily marked white) embedded in an amorphous material. (b) BF image shows the investigated agglomerated particles. (c) Diffraction pattern of the agglomerate reveals polycrystallinity of the reaction product. Diffraction rings fit to L-cystine and tetragonal as well as hexagonal Cu_2S.

are listed in ESI Table 1†). The same reflections were found in the XRD pattern (Fig. 6). $Cu^{II}S$ or Cu_xO was not observed.

EELS measurements in STEM confirmed the presence of Cu_2S or Cu^I, respectively. The S-$L_{2,3}$ and Cu-$L_{2,3}$ edges in the spectra show similarities to the one of Cu_2S when compared with data from the literature (Fig. 8).[48] For the heated sample, the EELS spectra show characteristics of CuS or Cu^{II}, respectively.

Discussion

In Table 2 the results for the three synthesized films A, B and C are summarized. For all the films the ratio between Cu and In precursor was fixed at 1 : 1 while the S content was varied. For film A the highest amount of sulfur was used (the concentration of the other precursors was adjusted), whereas for film B and C only the molarity was changed.

The different film thicknesses can be explained with the use of different reactant concentrations. For the highest molar concentration of precursors in film A the largest film thickness of 1.6 μm can be obtained. For film B and C with a lower molarity the film thickness is lower. These two films were synthesized with the same sulfur to copper/indium ratio but a higher molarity for film B compared to film C. This results only in a higher thickness for film B compared to C while the morphology of the films stays the same (compact nanoparticle film). Due to the higher amount of sulfur for sample A the surface topography was changed and a surface structure

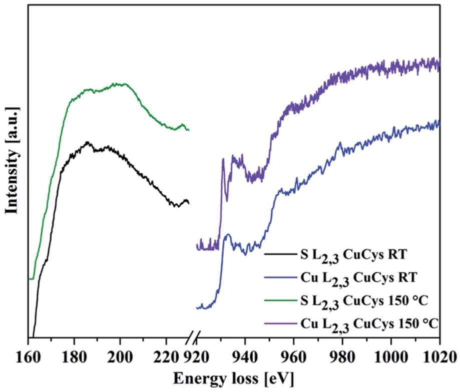

Fig. 8 EELS spectra taken from the product of L-cysteine and $CuSO_4$. The obtained S-$L_{2,3}$ and Cu-$L_{2,3}$ edges for the product stirred at RT for 18 h (bottom curves, black and blue) indicate the presence of Cu^+ when compared with literature.[48] The ones taken from the product synthesized for 18 h at 150 °C show differences, which indicate the formation of Cu^{2+} (upper curves, green and violet) when compared to literature spectra.[48]

consisting of interconnected nanoflakes was synthesized. By applying the Scherrer equation[32] on the obtained XRD pattern an average crystallite size of 10 ± 1 nm was calculated for all the films. However, analysis of the HR-TEM data resulted in smaller crystal sizes. Film A consists of crystals up to 6.3 ± 2.6 nm, film B (with a lower reactant concentration) of crystals up to 5.3 ± 2.2 nm, and for film C an average crystallite size of 4.9 ± 2.0 nm was determined. All crystal sizes are rather similar but it seems that the lower the S content in the precursor solution (film A > film C > film B) the smaller the crystals (film A > film B > film C). Therefore it can be concluded that during the reaction the film starts to grow with $CuInS_2$ nuclei of similar size to form a polycrystalline compact film consisting of small nanoparticles. Dependent on the amount of precursor salts, more or fewer crystals are formed in the reaction solution and as a consequence there are more and larger agglomerates on top of this compact layer for higher precursor concentrations (film B > film C).

It is well known that $CuInS_2$ can be both a p- or an n-type semiconductor dependent on the chemical composition.[4] For stoichiometric, Cu-rich as well as S-rich compositions p-type conductivity can be obtained.[49,50] Only In-rich $CuInS_2$ shows n-type conductivity.[51] The EDX data obtained in STEM mode show slightly higher S content for film B, which should improve the p-type conductivity of $CuInS_2$.[49] For film C a small lack of In can be obtained with EDX in STEM which should also lead to an improved p-type conductivity.[49,50] Film A has a completely different structure compared to films B and C. (S)TEM showed two distinct layers. For the surface layer, consisting of nanoflakes and rods, EDX revealed mainly the presence of sulfur and indium. This is in accordance to electron diffraction where the formation of In_2S_3 was also proven. The bottom layer, however, showed a roughly stoichiometric $CuInS_2$ composition with only slightly higher In and S amounts. Higher In amount can lead to n-type semiconductivity in $CuInS_2$ [51] and In_2S_3 is a known n-type semiconductor.[35] The combination of $CuInS_2$ and In_2S_3 for *e.g.* solar cells or water splitting is also already known in literature.[52,53] The synthesis of both materials at the same time seems to be promising for future applications.

UV-Vis measurements show a close to linear dependence of absorbance on the film thickness. For film A with the highest film thickness of 1.6 μm, the absorbance is fourfold compared to the thinner films B and C, which have a thickness of 300–500 nm. Nevertheless, all the films show significant absorption over the whole visible spectrum, which is a prerequisite for the use in solar-driven applications. Investigations of the band gaps, using the Tauc plot for direct band gap semiconductors, resulted in band gaps close to the value of 1.5 eV for the bulk material.[1] The calculated band gaps are 1.43 eV for film A, 1.47 eV for film B and 1.40 eV for film C, respectively. Decreasing of the band gap could be due to the polycrystallinity and related band gap states. Polycrystallinity implies that a large number of defects, *e.g.* grain boundaries, are present which can lead to sub-band excitations (*e.g.* Urbach tails, see Fig. 3). In addition, the different chemical composition can affect the band gap values.

To understand the formation of $CuInS_2$ *via* the L-cysteine assisted solvothermal synthesis in more detail, we performed additional experiments. On the one hand, $CuSO_4$ and L-cysteine were stirred in ethanol for 18 h at RT (ratio Cu : S 1 : 2.5, molarity 0.02 M : 0.05 M), on the other hand the reaction solution was heated to 150 °C for 18 h.

A redox reaction takes place when L-cysteine (the sulfur source) reacts with Cu^{II} ions from the aqueous $CuSO_4$ solution to Cu^I, while the thiols are oxidized to disulfides (L-cystine, see Fig. 9). Cu^I can interact with the excess thiols. In addition, due to

Table 2 Summarized results of the synthesized films A, B and C

	Film A	Film B	Film C
Cu : In : S molarity [M]	0.03 : 0.03 : 1.2	0.02 : 0.02 : 0.05	0.01 : 0.01 : 0.03
Nominal Cu : In : S precursor ratio	1 : 1 : 4	1 : 1 : 2.5	1 : 1 : 3
Film thickness [nm]	1600	450	350
Crystallite size XRD [nm]	10 ± 1	10 ± 1	10 ± 1
Band gap [eV]	1.43	1.47	1.40
Cu : In : S EDX TEM	1.0 : 3.0 : 4.8 1.0 : 1.3 : 2.3	1.0 : 1.0 : 2.1	1.0 : 0.9 : 2.0
Crystallite size TEM [nm]	6.3 ± 2.6	5.3 ± 2.2	4.9 ± 2.0
Proposed conductivity type	n	p	p

favorable soft-acid/base interactions a Cu^{I} cysteine complex can be formed. This mechanism is reported in the literature.[25,46,54,55]

Li *et al.*[25] synthesized CuS nanoparticles from $CuCl_2$ and L-cysteine by a hydrothermal method (160 °C, 12 h). They used different ratios of L-cysteine to $CuCl_2$ (1 : 1, 2 : 1, 3 : 1) and observed particles with different morphologies (ranging from microspheres to flakes). For the highest ratio of L-cysteine to $CuCl_2$ (3 : 1) precipitates were formed in the precursor solution after 15 min of stirring at room temperature. Their investigation showed that these precipitates consist of Cu^{I} cysteine complexes and cystine. After the redox reaction between L-cysteine and the Cu^{II} ions from the precursor salt, which leads to Cu^{I} and cystine, complexes are formed which stabilize the Cu^{I}. No Cu^{2+} ions were left after the reaction. During hydrothermal treatment, sulfur is released from L-cysteine and Cu^{I} is oxidized.[56] Consequently, Cu^{II}S is formed as the product.

Comparing the results from Li *et al.*[25] with our reaction system, we can derive a similar mechanism: when stirring L-cysteine with $CuSO_4$ at a ratio of 2.5 : 1 for 18 h at room temperature, we observe a grey solid, which consists not only of cystine and Cu^{I} and Cu^{II} cysteine complexes but also of Cu_2S particles. Cu_2S particles were formed in our case because of the long stirring and thus beginning decomposition of the S–S bonds of the cystine molecules and release of S from the remaining L-cysteine. Hence, the sample where L-cysteine and $CuSO_4$ in ethanol were heated for 18 h at 150 °C gave only hexagonal CuS (see XRD pattern in Fig. 6(b) and 8).

During the solvothermal $CuInS_2$ synthesis reactions occur similar to those mentioned above. Free In^{3+} can react with S^{2-}, which stems from the decomposition of L-cysteine and L-cystine, to form dissolved $(InS_2)^-$. The latter mechanism has been observed in literature in similar systems.[17,31,57] The $(InS_2)^-$ can react with Cu^+ in solution to form the ultimate product $CuInS_2$. The L-cysteine complexes stabilize the Cu^{I} until enough sulfur is released from cystine to form $(InS_2)^-$, which can react with Cu^{I}. After reacting with $(InS_2)^-$, $CuInS_2$ is formed. Li *et al.*[25] observed a higher amount of Cu^{II} ions in their precursor with a lower L-cysteine to $CuCl_2$ ratio of 2 : 1. In contrast, we did not found any Cu^{II} containing phases. Therefore we can conclude that for our synthesis pathway a ratio of S : Cu of 2.5 : 1 is already sufficient to suppress the formation of Cu^{II}S phases. Because the S : Cu ratio is higher for all our films (precursor ratio A: 4 : 1, B: 2.5 : 1, C: 3 : 1) this should be true also for the other films.

As already mentioned above, the (Cu–In–S)-system can be described with the help of the quasi-binary Cu_2S–In_2S_3 phase diagram. This phase diagram indicates the formation of mainly $CuInS_2$ in the chalcopyrite structure at around 50 to 52% mole percent In_2S_3.[41] In our reaction we use Cu : In at equimolar composition, so the formation of $CuInS_2$ in the chalcopyrite structure is plausible and can be supported with the XRD and electron diffraction data.

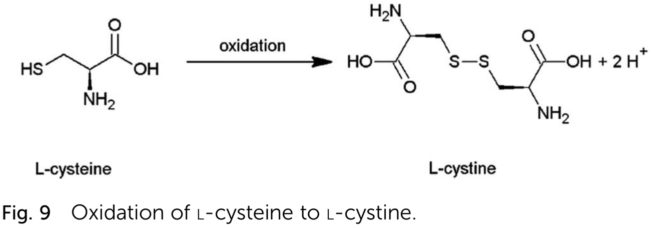

Fig. 9 Oxidation of L-cysteine to L-cystine.

The reason for the morphology of film A with the highest Cu : In : S precursor ratio of 1 : 1 : 4 consisting of a compact $CuInS_2$ bottom layer and a flaky In_2S_3 surface layer is related to the high L-cysteine amount. More L-cysteine means more Cu–cysteine/cystine complexes and therefore less free Cu ions. Due to the high S amount a lot of free S^{2-} ions are available beside the free In^{3+}. The formation of In_2S_3 out of $InCl_3$ and L-cysteine is reported in literature.[35] Interestingly, the here synthesized film has the same appearance as $CuInS_2$ films solvothermally synthesized with thioacetamide as sulfur source.[15]

Additionally, we note that we only use L-cysteine as reducing species while in literature studies additional reducing agents such as ethylenediamine and *N*,*N*-dimethylformamide (DMF) have been added.[17,31]

As mentioned above, Wen *et al.*[31] synthesized $CuInS_2$ powder with L-cysteine as sulfur source and DMF as a solvent. They obtained microspheres made up of nanosheets with varying sheet thickness from 50 to 100 nm. They proposed that Cu^{II} was reduced to Cu^{I} by the solvent DMF. Despite using a different Cu source and solvent, a powder with similarly composed nanospheres was obtained during our reaction in addition to the films in the autoclave.

Liu *et al.*[17] also synthesized $CuInS_2$ nanocrystals *via* an L-cysteine-assisted solvothermal process. Using ethylene diamine : water 1 : 1 as solvent, a product of agglomerates of irregular microspheres and nanocrystals was obtained. The SEM study of their product shows a structure of nanocrystals similar to the SEM top view of our film B (Fig. 1(d)). XRD data revealed the tetragonal chalcopyrite structure, which was confirmed using electron diffraction patterns obtained in the TEM in accordance to our studies.

To summarize, the solvothermally grown $CuInS_2$ films synthesized in this study show promising properties: suitable band gaps for solar-driven applications, an interesting nanostructure and good crystallinity. First dye degradation tests with the dye rhodamine B show that the films are active under solar illumination (see ESI Fig. 3†).

Conclusion

In this study L-cysteine was used for the first time to prepare $CuInS_2$ thin films on FTO *via* a cost-efficient solvothermal synthesis route with low toxicity. It is shown that L-cysteine is able to reduce Cu^{II} from the used $CuSO_4$ precursor in aqueous solution to Cu^{I} to induce the formation of $CuInS_2$. All three resulting $CuInS_2$ films, synthesized with different concentrations of reactants, show different film thicknesses, slightly different grain sizes and vary in chemical composition dependent on the amount of sulfur used. The microstructural investigations reveal a polycrystalline compact layer for all films, except for the film with the highest amount of sulfur which shows an additional surface layer consisting of interconnected nanoflakes. EDX measurements show nearly stoichiometric composition of the films but for the nanoflake layer a drastically In rich composition. This is accordance to electron and X-ray diffraction data which reveal that the flakes crystallize as In_2S_3 while the compact films show the characteristic reflections of $CuInS_2$ in the chalcopyrite structure. Moreover, all three films A, B and C show significant optical absorption over the whole visible spectrum and offer suitable band gaps for solar energy applications. The band gap value depends on the composition as well as on the grain size. The films are viewed as possible candidates for absorber layers in solar cells or photoelectrochemical cells, especially the combination of $CuInS_2$ and In_2S_3 can be very interesting. First dye degradation tests under solar illumination show promising activity of the films.

Acknowledgements

Financial support from the cluster of excellence Nanosystems Initiative Munich (NIM) is gratefully acknowledged. The authors thank Benjamin Breitbach and Sophia Betzler for technical support.

References

1 B. Tell, J. L. Shay and H. M. Kasper, *Phys. Rev. B: Solid State*, 1971, **4**, 2463–2471.

2 F. M. Courtel, R. W. Paynter, B. Marsan and M. Morin, *Chem. Mater.*, 2009, **21**, 3752–3762.

3 C.-W. Chen, D.-Y. Wu, Y.-C. Chan, C. C. Lin, P.-H. Chung, M. Hsiao and R.-S. Liu, *J. Phys. Chem. C*, 2015, **119**, 2852–2860.

4 D. C. Look and J. C. Manthuruthil, *J. Phys. Chem. Solids*, 1976, **37**, 173–180.

5 J. A. Hollingsworth, K. K. Banger, M. H. C. Jin, J. D. Harris, J. E. Cowen, E. W. Bohannan, J. A. Switzer, W. E. Buhro and A. F. Hepp, *Thin Solid Films*, 2003, **431–432**, 63–67.

6 M. C. Zouaghi, T. B. Nasrallah, S. Marsillac, J. C. Bernède and S. Belgacem, *Thin Solid Films*, 2001, **382**, 39–46.

7 S. i. Kuranouchi and T. Nakazawa, *Sol. Energy Mater. Sol. Cells*, 1998, **50**, 31–36.

8 H. M. Pathan and C. D. Lokhande, *Appl. Surf. Sci.*, 2004, **239**, 11–18.

9 Y. Shi, Z. Jin, C. Li, H. An and J. Qiu, *Appl. Surf. Sci.*, 2006, **252**, 3737–3743.

10 H. Liu, C. Gu, W. Xiong and M. Zhang, *Sens. Actuators, B*, 2015, **209**, 670–676.

11 J. Guo, G. Chang, W. Zhang, X. Liu and Y. He, *Chem. Phys. Lett.*, 2016, **647**, 51–54.

12 M. H. Amerioun, M. E. Ghazi, M. Izadifard and B. Bahramian, *Eur. Phys. J. Plus*, 2016, **131**, 1–9.

13 S. Peng, F. Cheng, J. Liang, Z. Tao and J. Chen, *J. Alloys Compd.*, 2009, **481**, 786–791.

14 Y. Zhao, F. Luo, M. Zhuang, Z. Liu, A. Wei and J. Liu, *Appl. Phys. A*, 2016, **122**, 1–7.

15 A. Wochnik, C. Heinzl, F. Auras, T. Bein and C. Scheu, *J. Mater. Sci.*, 2012, **47**, 1669–1676.

16 A. S. Wochnik, A. Frank, C. Heinzl, J. Häusler, J. Schneider, R. Hoffmann, S. Matich and C. Scheu, *Solid State Sci.*, 2013, **26**, 23–30.

17 H.-T. Liu, J.-S. Zhong, B.-F. Liu, X.-J. Liang, X.-Y. Yang, H.-D. Jin, F. Yang and W.-D. Xiang, *Chin. Phys. Lett.*, 2011, **28**, 057702.

18 C. F. Monson and A. T. Woolley, *Nano Lett.*, 2003, **3**, 359–363.

19 Q. Lu, F. Gao and S. Komarneni, *J. Am. Chem. Soc.*, 2003, **126**, 54–55.

20 X. Chen, X. Zhang, C. Shi, X. Li and Y. Qian, *Solid State Commun.*, 2005, **134**, 613–615.

21 M. C. Brelle, J. Z. Zhang, L. Nguyen and R. K. Mehra, *J. Phys. Chem. A*, 1999, **103**, 10194–10201.

22 J. Xiang, H. Cao, Q. Wu, S. Zhang, X. Zhang and A. A. R. Watt, *J. Phys. Chem. C*, 2008, **112**, 3580–3584.

23 B. Zhang, X. Ye, W. Hou, Y. Zhao and Y. Xie, *J. Phys. Chem. B*, 2006, **110**, 8978–8985.

24 P. Zhao, T. Huang and K. Huang, *J. Phys. Chem. C*, 2007, **111**, 12890–12897.

25 B. Li, Y. Xie and Y. Xue, *J. Phys. Chem. C*, 2007, **111**, 12181–12187.

26 J. Xiang, H. Cao, Q. Wu, S. Zhang and X. Zhang, *Cryst. Growth Des.*, 2008, **8**, 3935–3940.

27 J. Zhong, W. Xiang, C. Xie, X. Liang and X. Xu, *Mater. Chem. Phys.*, 2013, **138**, 773–779.

28 Y. Tao, N. Cao, J. Pan, Y. Sun, C. Jin and Y. Song, *J. Mater. Sci.*, 2014, **49**, 897–904.

29 C. Wen, W. Aiwu, R. Tingke, H. Jie, F. Li, Z. Jiasong and X. Weidong, *Micro Nano Lett.*, 2015, **10**, 45–49.

30 J. Zhong, Q. Wang and W. Cai, *Mater. Lett.*, 2015, **150**, 69–72.

31 C. Wen, X. Weidong, W. Juanjuan, W. Xiaoming, Z. Jiasong and L. Lijun, *Mater. Lett.*, 2009, **63**, 2495–2498.

32 P. Scherrer, *Nachr. Ges. Wiss. Goettingen, Math.-Phys. Kl.*, 1918, **26**, 3.

33 J. Tauc and A. Menth, *J. Non-Cryst. Solids*, 1972, **8–10**, 569–585.

34 B. Koo, R. N. Patel and B. A. Korgel, *Chem. Mater.*, 2009, **21**, 1962–1966.

35 L. Zhang, W. Zhang, H. Yang, W. Fu, W. Zhao, H. Zhao and J. Ma, *Mater. Chem. Phys.*, 2011, **130**, 932–936.

36 M. Benchikhi, R. El Ouatib, L. Er-Rakho and B. Durand, *Ceram. Int.*, 2016, **42**, 11303–11308.

37 K. Das, S. K. Panda, S. Gorai, P. Mishra and S. Chaudhuri, *Mater. Res. Bull.*, 2008, **43**, 2742–2750.

38 J. H. Werner, J. Mattheis and U. Rau, *Thin Solid Films*, 2005, **480–481**, 399–409.

39 S. Siebentritt, *Sol. Energy Mater. Sol. Cells*, 2011, **95**, 1471–1476.

40 A. Lafond, X. Rocquefelte, M. Paris, C. Guillot-Deudon and V. Jouenne, *Chem. Mater.*, 2011, **23**, 5168–5176.

41 J. J. M. Binsma, L. J. Giling and J. Bloem, *J. Cryst. Growth*, 1980, **50**, 429–436.

42 S. A. Moggach, D. R. Allan, S. Parsons, L. Sawyer and J. E. Warren, *J. Synchrotron Radiat.*, 2005, **12**, 598–607.

43 K. M. Dokken, J. G. Parsons, J. McClure and J. L. Gardea-Torresdey, *Inorg. Chim. Acta*, 2009, **362**, 395–401.

44 P. Lukashev, W. R. L. Lambrecht, T. Kotani and M. van Schilfgaarde, *Phys. Rev. B: Condens. Matter Mater. Phys.*, 2007, **76**, 195202.

45 A. Janosi, *Acta Crystallogr.*, 1964, **17**, 311–312.

46 K. M. Dokken, J. G. Parsons, J. McClure and J. L. Gardea-Torresdey, *Inorg. Chim. Acta*, 2009, **362**, 395–401.

47 H. Fjellvag, F. Gronvold, S. Stolen, A. F. Andresen, R. Mueller Kaefer and A. Simon, *Z. Kristallogr.*, 1988, **184**, 111–121.

48 F. Hofer and P. Golob, *Ultramicroscopy*, 1987, **21**, 379–383.

49 H. Bihri and M. Abd-Lefdil, *Thin Solid Films*, 1999, **354**, 5–8.

50 B. Tell, J. L. Shay and H. M. Kasper, *J. Appl. Phys.*, 1972, **43**, 2469–2470.

51 N. H. Y. H. J. Hsu, R. S. Tang, T. M. Hsu and H. L. Hwang, *J. Cryst. Growth*, 1984, **20**, 83.

52 T. Theresa John, M. Mathew, C. Sudha Kartha, K. P. Vijayakumar, T. Abe and Y. Kashiwaba, *Sol. Energy Mater. Sol. Cells*, 2005, **89**, 27–36.

53 Gunawan, W. Septina, S. Ikeda, T. Harada, T. Minegishi, K. Domen and M. Matsumura, *Chem. Commun.*, 2014, **50**, 8941–8943.

54 D. Cavallini, C. De Marco, S. Duprè and G. Rotilio, *Arch. Biochem. Biophys.*, 1969, **130**, 354–361.

55 M. Ahmed, M. S. Iqbal, N. Tahir and A. Islam, *World Appl. Sci. J.*, 2011, **14**, 210–214.

56 P. Roy and S. K. Srivastava, *Cryst. Growth Des.*, 2006, **6**, 1921–1926.

57 A. Kharkwal, S. N. Sharma, K. Jain and A. K. Singh, *Mater. Chem. Phys.*, 2014, **144**, 252–262.